

GRB 050713A: High Energy Observations of the GRB Prompt and Afterglow Emission

D.C. Morris¹, J. Reeves², V. Pal'shin³, M. Garczarczyk⁴, A.D. Falcone¹, D.N. Burrows¹, H. Krimm², N. Galante⁵, M. Gaug⁶, S. Golenetskii³, S. Mizobuchi⁴, C. Pagani¹, A. Stamerra⁵, M. Teshima⁴, A.P. Beardmore⁷, O. Godet⁷, N. Gehrels²

ABSTRACT

Swift discovered GRB 050713A and slewed promptly to begin observing with its narrow field instruments 72.6 seconds after the burst onset, while the prompt gamma-ray emission was still detectable in the BAT. Simultaneous emission from two flares is detected in the BAT and XRT. This burst marks just the second time that the BAT and XRT have simultaneously detected emission from a burst and the first time that both instruments have produced a well sampled, simultaneous dataset covering multiple X-ray flares. The temporal rise and decay parameters of the flares are consistent with the internal shock mechanism. In addition to the *Swift* coverage of GRB 050713A, we report on the Konus-Wind (K-W) detection of the prompt emission, an upper limiting GeV measurement of the prompt emission made by the MAGIC imaging atmospheric Cherenkov telescope and *XMM-Newton* observations of the afterglow. Simultaneous observations between *Swift* XRT and *XMM-Newton* produce consistent results, showing a break in the lightcurve at $T_0 + \sim 15$ ks. Together, these four observatories provide unusually broad spectral coverage of the prompt emission and detailed X-ray follow-up of the afterglow for two weeks after the burst trigger. Simultaneous spectral fits of K-W with BAT and BAT with XRT data indicate that an absorbed broken powerlaw is often a better fit to GRB flares than a simple absorbed powerlaw.

¹Department of Astronomy & Astrophysics, 525 Davey Lab., Pennsylvania State University, University Park, PA 16802, USA; morris@astro.psu.edu

²NASA/Goddard Space Flight Center, Greenbelt, MD 20771, USA

³Ioffe Physico-Technical Institute

⁴Max-Planck-Institut für Physik, München, Germany

⁵Dipartimento di Fisica, Università di Siena, and INFN Pisa, Italy

⁶Institut de Física d'Altes Energies, Barcelona, Spain

⁷Department of Physics and Astronomy, University of Leicester, Leicester, LE1 7RH, UK

These spectral results together with the rapid temporal rise and decay of the flares suggest that flares are produced in internal shocks due to late time central engine activity.

Subject headings: gamma rays: bursts

1. Introduction

The *Swift* Gamma-Ray Burst Explorer (Gehrels et al., 2004) has been returning unprecedented data about gamma ray bursts (GRBs) for the past 18 months. Of particular interest in the bursts followed by *Swift* have been the early time lightcurves of the afterglows which have shown much greater structure and different temporal decay properties than expected, leading to much discussion in the literature regarding the nature of the transition between the prompt emission, thought to be due to synchrotron radiation from internal collisions (Gallant et al., 1999), and the afterglow, also thought to be due to synchrotron radiation, though it remains somewhat unclear whether the emission arises in internal or external shocks. *Swift* observations have shown that GRB lightcurves can be described by a canonical 3-segment shape. This shape consists of 1 - an early steep decay phase ($F_\nu \propto \nu^{-\beta} t^{-\alpha}$ where $3 \leq \alpha_1 \leq 5$; $t < 500$ s) 2 - a very shallow decay phase ($0.5 \leq \alpha_2 \leq 1.0$; 500 s $< t < 10^4$ s) and 3 - a 'normal' decay phase ($1 \leq \alpha_3 \leq 1.5$; 10^4 s $< t$) (Nousek et al., 2005). Superimposed on this smooth decay profile, *Swift* has shown that bright x-ray flares, 2 to 100 times as bright as the underlying afterglow, are common during the early ($t \leq 10$ ks) stages of GRBs (Burrows et al., 2005b; Falcone et al., 2006; Piro 2005b; Romano et al., 2005).

The observation of GRB050117 (Hill et al., 2005) marked the first time that *Swift* slewed to and settled on a GRB while the prompt gamma ray emission was still in progress, arriving 192 seconds after the Burst Alert Telescope (BAT) triggered on the burst which had a T_{90} of 168 seconds. Due to irregularities in the observing mode of the XRT and the proximity of the South Atlantic Anomaly to *Swift* during the observation of GRB050117, however, only very sparse data was collected by the XRT, totaling 11.4 seconds in the first orbit and 946 seconds overall. This left large gaps in the lightcurve coverage and severely limited the quality of the spectral analysis that could be performed.

We report here on the observation of GRB 050713A (Falcone et al., 2005), a burst of $T_{90} = 70$ seconds to which *Swift* slewed and began collecting data with the narrow field instruments (NFIs) in just 72.6 seconds, while the prompt gamma ray emission was still detectable by the BAT. This burst marks just the second time that the BAT and XRT have

collected simultaneous data on a burst and it marks the first time that both instruments have produced a well sampled, simultaneous dataset covering multiple flares in the prompt emission.

In addition to the *Swift* coverage of GRB 050713A, we report also on prompt and followup observations carried out by Konus-Wind, MAGIC, *XMM-Newton* and ground based optical observatories. In section 2 we describe the observations and data analysis from all instruments including ground follow-up. In section 3 we discuss the implications of the observations in light of the new theoretical understanding emerging from *Swift* observations of GRBs. In section 4 we summarize and present our conclusions. Quoted uncertainties are at the 90% confidence level for one interesting parameter (i.e., $\Delta\chi^2=2.71$) unless otherwise noted.

2. Observations and Data Analysis

Many different observatories and instruments have observed GRB 050713A. We devote the following section to a description of the observations and analysis carried out by each instrument team. All spectral fits were performed using XSPEC v11.3.

2.1. *Swift* BAT

The *Swift* BAT (Barthelmy et al., 2005) triggered on GRB 050713A at 04:29:02.39 UT, measuring a peak 1-second flux of 6.0 ± 0.4 photons $\text{cm}^{-2} \text{ s}^{-1}$. T_{90} measured in the 15–350 keV energy range is 70 ± 10 s (Palmer et al., 2005). The onset of the burst as defined by the BAT trigger is preceded by a weak, hard (photon index = 1.26) precursor at T_0-60 s. BAT data were processed using the BAT ground software build 11 and BAT Calibration Database files build 11.

At the time of the BAT trigger, the flux rose rapidly and remained elevated during a 12 s long, multipeaked burst (Fig 1). At T_0+12 s, the BAT flux rapidly decayed with a powerlaw decay rate of $\alpha \sim 8$ for 5 seconds before breaking to a more shallow decay of $\alpha \sim 2.5$ at T_0+17 s. This decay continued until T_0+40 s at which point the BAT flux had decayed to near background levels. At T_0+50 s, a flare is seen with peak flux 2×10^{-8} ergs $\text{cm}^{-2} \text{ s}^{-1}$, extrapolated into the XRT 0.2–10.0 keV bandpass, followed by a flare with peak flux 3.5×10^{-8} ergs $\text{cm}^{-2} \text{ s}^{-1}$ at T_0+65 s, another at T_0+105 s with peak flux 1×10^{-8} ergs $\text{cm}^{-2} \text{ s}^{-1}$ and some hint of further emission at the onset of a flare seen in the XRT at T_0+160 s. A weak but statistically significant precursor is seen at T_0-70 s to

T_0 –50 s followed by a period of no significant emission from T_0 –50 s to the burst trigger.

The spectrum of the entire BAT dataset is well fit by a power-law spectrum with photon index = 1.58 ± 0.07 , though there is evidence for a slightly harder index of 1.45 during the plateau and a softening to $\Gamma = 1.60$ during the rapid decay, and further softening to $\Gamma = 2.0$ during the weak flares. Using the global fit of $\Gamma = 1.58$, the fluence is $9.1 \pm 0.6 \times 10^{-6}$ ergs cm $^{-2}$ in the 15–350 keV energy range.

2.2. Konus-Wind

GRB 050713A triggered Konus-Wind (K-W) (Aptekar et al., 1995) at T_0 (K-W)=04:29:01.745 UT. It was detected by the S2 detector, which observes the north ecliptic hemisphere, with an incident angle of $18^\circ 1$. The K-W lightcurve in 3 bands is shown in Figure 2. The propagation delay from Wind to *Swift* is 1.387 s for this GRB. Correcting for this factor, one sees that the K-W trigger time corresponds to $T_0 + 0.742$ s. Prior to T_0 (K-W)–0.512 s data were collected by K-W in a survey mode with lower time resolution of 2.944 s and only 3 broad spectral channels, 18–70 keV, 70–300 keV and 300–1160 keV. From T_0 (K-W) to T_0 (K-W)+491.776 s, 64 spectra in 101 channels were accumulated on time scales varying from 64 ms near the trigger to 8.19 s by the time the signal became undetectable. The multichannel spectra cover the 18 keV–14 MeV energy range but no statistically significant emission is seen above 2 MeV. Data were processed using standard Konus-Wind analysis tools.

Joint spectral analysis was carried out using the BAT data between 15 and 150 keV and the KONUS data from 20 to 2000 keV. The spectra were fit by a power law model with an exponential cut off: $dN/dE \propto E^{-\alpha} e^{-(2-\alpha)E/E_p}$ where E_p is the peak energy of the νF_ν spectrum and α is the photon index. The spectrum of the main pulse is well fit (Fig 3) with photon index = 1.26 ± 0.07 and $E_p = 421^{+119}_{-80}$ keV ($\chi^2 = 138/119$ dof). Joint fits between BAT and Konus were also made for other time intervals, including one which shows the faint precursor detected by both instruments at $T_0 \sim -60$ s, and will be addressed in greater detail in section 3.3.

The main pulse fluence in the 20 keV to 2 MeV range is $8.08^{+0.55}_{-1.77} \times 10^{-6}$ erg cm $^{-2}$. The 256-ms peak flux measured from $T_0 + 1.2$ s in the 20 keV to 2 MeV band is $1.34^{+0.11}_{-0.45} \times 10^{-5}$ erg cm $^{-2}$ s $^{-1}$ and the T_{90} durations of the burst in the G1, G2, G3 energy bands are 17 ± 2 s, 14 ± 4 s and 12 ± 2 s, respectively.

2.3. *Swift* XRT

The XRT (Burrows et al., 2005a) performs an automated sequence of observations (Hill et al., 2004) after *Swift* slews to a GRB detected by the BAT. When the spacecraft first settles on the target, a short image (0.1 s followed by a longer 2.5 s image if a position is not determined in 0.1 s) is taken to determine an accurate position. Following the image, the XRT switches into either Windowed Timing (WT) mode (a high timing accuracy mode with 1 dimensional position information) if the source count rate is above 2 counts s^{-1} , or Photon Counting (PC) mode (the more traditional operating mode of X-ray CCDS in which full 2 dimensional position information is retained but with only 2.5 s timing resolution) if the count rate is below 2 counts s^{-1} .

XRT collected a 0.1 s Image Mode frame upon settling on GRB 050713A 73 seconds after the BAT trigger, which yields a count rate of 314 counts s^{-1} . Following the Image Mode frame, XRT cascaded down through its automated mode sequence and collected its first WT frame 4.5 seconds later. At the onset of the WT data, the XRT count rate was about 100 counts s^{-1} and decaying as a powerlaw. This initial powerlaw decay in the XRT WT data together with the Image Mode data point measured at a flux level ~ 3 times higher just 4.6 s earlier clearly indicates that the XRT settled and began taking data during the latter portion of the flare detected in the BAT at T_0+65 seconds (see Fig 4). XRT remained in WT mode throughout the entire first orbit of data collection on GRB 050713A, also observing the flare detected by the BAT at T_0+105 and a lower level flare not clearly detected by the BAT at T_0+155 s.

Following a 65 minute period of occultation by the Earth, XRT began observations again at T_0+4300 s, now observing in PC mode since the countrate of the source had decayed below 2 counts s^{-1} . A small flare at T_0+10 ks and the indication of another flare at T_0+45 ks are seen in the late time XRT lightcurve data, superimposed on an otherwise steady powerlaw decay. XRT observations continue to monitor the source until $T_0+1.8\times 10^6$ s, a total exposure time of 178 ks, at which time the source had decayed below the XRT detection threshold.

XRT data are processed using the *xrtpipeline* ground software version 0.9.9, the redistribution response matrices `swxwt0to2_20010101v007.rmf` (WT data) and `swxpc0to12_20010101v007.rmf` (PC data), and ancillary response files generated with the *xrtpipeline* task `xrtmkarf`.

2.3.1. XRT GRB Position Analysis

The X-ray afterglow position determined from ground processing of the data is RA(J2000) = $21^{\text{h}}22^{\text{m}}9\overset{\text{s}}{.}8$ Dec(J2000) = $+77^{\circ}4'29''$ 0 with an uncertainty of 3.2 arcseconds.

This is 10.5 arcseconds from the reported BAT position, 0.5 arcseconds from the optical counterpart reported by Malesani et al., (Malesani et al., 2005) and 1.5 arcseconds from the initial XRT position calculated onboard the satellite and automatically distributed via the GCN network (Falcone et al., 2005). An X-ray image compiled from the first segment of XRT PC data is shown as Figure 5 with the BAT, XRT and optical counterpart error circles displayed. A faint background source is detected 30 arcseconds due south of the GRB afterglow at a constant flux level of $7 \pm 2 \times 10^{-4}$ counts s $^{-1}$. The contribution of this steady source has been removed from the calculation of the afterglow lightcurve.

2.3.2. XRT Temporal Analysis

A timeline of the XRT (as well as other) observations of GRB 050713A is shown in Table 1. The lightcurve will be broadly treated in two parts. The first part is the initial orbit of data, during which the lightcurve is characterized by bright flares which are simultaneously observed by the BAT as well as the K-W instrument at higher energies. Due to the extreme variability in this portion of the lightcurve, a global decay index cannot be determined from the XRT data. The second part is the remainder of the XRT data from the second orbit onward, which is characterized primarily by a broken powerlaw decay, though at least one small flare is seen superimposed atop this global decay.

First Orbit

Swift finished slewing to GRB 050713A at T_0+73 s, during the flare which began at T_0+65 s. The XRT short image frame is collected just after the peak of this flare, at a flux of 1.2×10^{-8} ergs cm $^{-2}$ s $^{-1}$, and the first 20 frames of WT data record the decay of the flare. Fitting a simple powerlaw to this decay from T_0+79 s to T_0+100 s setting T_0 to be the BAT burst trigger time, we find a powerlaw index of 5.6 ± 1.8 (1σ). At T_0+105 s a new flare begins, which rises with a powerlaw index of 23.3 ± 4.5 for 5-10 s, flattens at the peak of $\sim 9 \times 10^{-9}$ ergs cm $^{-2}$ s $^{-1}$ for 5-10 s, then decays with a more shallow powerlaw index of 8.4 ± 1.7 for about 30 s. At T_0+165 s a third flare is detected, which rises with a powerlaw slope of 8.9 ± 3.1 for 5-10 s, flattens at the peak of $\sim 1.5 \times 10^{-9}$ ergs cm $^{-2}$ s $^{-1}$ for 5-10 s, then decays with a slope of 6.1 ± 1.1 for 70 s before the end of the observing window due to Earth occultation.

Second Orbit and Later

The second orbit of data in the XRT is the only single orbit of data in which the afterglow is characterized by a well sampled (greater than 100 events total) lightcurve devoid of any obvious flaring activity. During the 1600 seconds of data in this orbit, from T_0+4360 s to T_0+5952 s, the lightcurve decays steadily as a powerlaw with decay index of about 1.0. The third orbit of data is characterized by another flare, beginning at T_0+10 ks, lasting throughout the entire orbit (about 2 ks) and reaching a peak flux of 1×10^{-11} ergs cm $^{-2}$ s $^{-1}$. A powerlaw fit to the rising portion of the flare yields a slope of 5.8 ± 1.8 while the decaying portion yields a slope of 11.0 ± 2.5 . This flare seems to be superposed atop the underlying afterglow decay of decay index $\alpha \sim 1$. Observations were interrupted after 150 s during the fourth orbit due to the occurrence of GRB 050713B, and observations of GRB 050713A remained suspended until T_0+40 ks. Some suggestion of another flare is seen in the orbit of data beginning at T_0+45 ks, though the statistics are poor. While afterglow data from the XRT alone do not clearly require a break in the afterglow powerlaw, *XMM-Newton* data (see §2.4) from T_0+21 ks to T_0+50 ks provide an accurate measure of the late-time decay slope ($\alpha = 1.45$) which cannot fit the XRT data from orbits 2 and 3 without a break in the powerlaw. The joint XRT-*XMM-Newton* lightcurve will be further discussed in §2.4. Table 2 summarizes the flares and their temporal fits.

2.3.3. XRT Spectral Analysis

The XRT spectral analysis of this burst is somewhat complicated by the high degree of flaring activity seen. In all cases, spectra are binned to a minimum of 20 counts per bin in order to use χ^2 statistics. Fitting the entire first orbit of data, the spectrum is well fit by a highly absorbed powerlaw with photon index = 2.28 ± 0.04 and $N_H = 4.8 \pm 0.2 \times 10^{21}$ cm $^{-2}$, which is significantly above the galactic column (1.1×10^{21} cm $^{-2}$) in the direction of GRB 050713A. We are also able, due to the large number of counts in each of the early flares in the dataset, to fit a spectrum to both the rising and decaying portions of the flares. In doing so we see the typical hard to soft evolution of the flares (Zhang and Meszaros, 2004).

The second orbit of data shows a significantly different spectrum from the first, with a harder spectrum with photon index = 1.9 ± 0.13 and a lower value of $N_H = 3.1 \pm 0.43 \times 10^{21}$, possibly indicating a period of energy injection (Nousek et al., 2005). The third orbit is well fit by a softer powerlaw similar to that which fit the first orbit with photon index = 2.25 ± 0.23 and $N_H = 4.1 \pm 0.7 \times 10^{21}$.

During the period of overlapping coverage between *Swift* and *XMM-Newton*, XRT has 3.5 ks of exposure time at a mean countrate of $0.04 \text{ counts s}^{-1}$ for a total of about 150 events during the simultaneous observing period. Fitting a spectrum to this overlapping coverage yields a photon index = 1.9 ± 0.30 and $N_{\text{H}} = 4.0 \pm 0.15 \times 10^{21}$. The corresponding mean unabsorbed 0.2–10.0 keV flux during the overlap period as measured by XRT is $3.4 \pm 0.34 \times 10^{-12} \text{ ergs cm}^{-2} \text{ s}^{-1}$.

The data collected after the third orbit (i.e., after the temporal break in the lightcurve at $T_0 + \sim 20$ ks) are too sparse to justify fitting with higher order models, but a simple absorbed powerlaw fit yields a spectrum of photon index = 2.8 ± 0.6 with $N_{\text{H}} = 5.6 \pm 0.2 \times 10^{21}$. This is consistent with the x-ray photon index found in orbits 1 and 3 and is marginally softer than the photon index found during orbit 2 which, as noted above, suggests a period of energy injection.

2.4. *XMM-Newton*

XMM-Newton follow-up observations of GRB 050713A commenced $T_0 + 23.6$ ks (for the EPIC-PN) and $T_0 + 20.9$ ks (for the two EPIC-MOS cameras). The *XMM-Newton* data were processed with the EPPROC and EMPROC pipeline scripts, using the *XMM-Newton* SAS analysis package, version 6.5. A bright rapidly decaying source is detected near the aimpoint of all three EPIC detectors, localized at RA(J2000)= $21^{\text{h}}22^{\text{m}}9^{\text{s}}.4$ Dec(J2000)= $+77^{\circ}4'28".1$. The net exposures after screening and deadtime correction are 24.1 ks (PN) and 27.0 ks (MOS). All three EPIC cameras (PN and 2 MOS) were used in Full Window Mode with the medium filter in place.

Source spectra and lightcurves for all 3 EPIC cameras were extracted from circular regions of 20 arcseconds radius centered on the afterglow. Background data were taken from a 60 arcseconds circle on the same chip as the afterglow, but free of any X-ray sources. Fitting the afterglow lightcurve with a simple power-law decay results in a decay index of $\alpha = 1.45 \pm 0.05$. Several flares are present in the background lightcurve, so as a conservative check, we also excluded times where the background rate is $> 0.1 \text{ counts s}^{-1}$. The afterglow decay rate is then $\alpha = 1.39 \pm 0.09$, consistent with the above value. The decay rate from the MOS lightcurve (for the two detectors combined) is also consistent at $\alpha = 1.35 \pm 0.06$.

2.4.1. *XMM-Newton* Spectral Analysis

Afterglow and background spectra were extracted with the same regions used for the lightcurves, while ancillary and redistribution response files were generated with the SAS tasks ARFGEN and RMFGEN respectively. As with XRT data, source spectra were binned to a minimum of 20 counts per bin in order to use χ^2 statistics. The PN and MOS spectra were fitted jointly, allowing only the cross normalization to vary between the detectors, which is consistent within $< 5\%$. The two MOS spectra and responses were combined to maximize the signal to noise, after first checking that they were consistent with each other. The average net source count rates obtained over the whole observation are $0.58 \pm 0.01 \text{ counts s}^{-1}$ for the PN and $0.20 \pm 0.01 \text{ counts s}^{-1}$ per MOS module.

Allowing the absorption column to vary in the spectral fit results in a formally acceptable fit ($\chi^2/\text{dof} = 515/496$). The N_{H} obtained is $3.1 \pm 0.1 \times 10^{21} \text{ cm}^{-2}$, while the continuum photon index $= 2.07 \pm 0.04$. The time-averaged, unabsorbed, 0.2–10.0 keV flux obtained for the afterglow is $3.2 \times 10^{-12} \text{ erg cm}^{-2} \text{ s}^{-1}$. These values are consistent with the *Swift* XRT measurement obtained at the time of the *XMM-Newton* observation.

The *XMM-Newton* afterglow spectra were also sliced into three segments of approximately 8 ks in length, in order to search for any spectral evolution within the *XMM-Newton* observation. No change in the continuum parameters was found, all three spectral segments being consistent with photon index $= 2.1$ and $N_{\text{H}} = 3 \times 10^{21} \text{ cm}^{-2}$. The spectrum obtained from the PN detector and residuals to an absorbed power-law model (with $\Gamma = 2.08 \pm 0.02$ and $N_{\text{H}} = 3.2 \times 10^{21} \text{ cm}^{-2}$) are shown in Figure 6.

2.4.2. Joint *XMM-Newton* and *Swift* Modeling of the Late Time Afterglow

The power-law decay index obtained from the *XMM-Newton* observation ($\alpha = 1.4$) appears to be steeper than that obtained from the *Swift* XRT in orbit 2 ($\alpha = 1.0$). In order to compare between the *XMM-Newton* and *Swift* afterglow lightcurves, a combined lightcurve from the *XMM-Newton* and *Swift* observations was produced, scaling to the absorbed continuum fluxes measured in the 0.5–10 keV band. The joint *Swift* and *XMM-Newton* lightcurve is shown in Figure 7, zoomed to better display the region at which the lightcurve break occurs.

A single power-law decay slope of $\alpha = 1.20 \pm 0.02$ is an extremely poor fit to the lightcurve in this region, with a fit statistic of $\chi^2/\text{dof} = 201.2/65$. Indeed the lightcurve from T_0+4 ks until T_0+1000 ks can be better fitted with a broken power-law. There is a flat decay index of $\alpha = 1.02 \pm 0.07$ at early times and a steeper decay index of $\alpha = 1.45 \pm 0.06$

at later times, with the break in the decay occurring at $T_0 + 25 \pm 3$ ks. The fit statistic is then $\chi^2/\text{dof} = 90.2/59$. The remaining contribution towards the χ^2 originates from two small possible flares present near $T_0 + \sim 10$ ks and $T_0 + \sim 45$ ks.

2.5. MAGIC

The MAGIC Telescope (Mirzoyan et al., 2005) was able to observe part of the prompt emission phase of GRB 050713A as a response to the alert provided by *Swift*. The observation, at energies above 175 GeV, started at $T_0 + 40$ s, 20 s after reception of the alert. It overlapped with the prompt emission phase measured by *Swift* and K-W, and lasted for 37 min, until twilight. The observation window covered by MAGIC did not, however, contain the burst onset peak detected at keV-MeV energies, where the *Swift* and K-W spectra were taken. The same region of the sky was observed 48 hours after the burst onset, collecting an additional 49 minutes of data, which was used to determine the background contamination.

The MAGIC (*Major Atmospheric Gamma Imaging Cherenkov*) Telescope is currently the largest single-dish Imaging Air Cherenkov Telescope (IACT) in operation, with the lowest energy threshold (60 GeV at zenith, increasing with zenith angle). In its fast slewing mode, the telescope can be repositioned within ~ 30 s. In case of an alert by GCN, an automated procedure takes only a few seconds to terminate any pending observation, validate the incoming signal and start slewing toward the GRB position, as was the case for GRB 050713A.

Using the standard analysis, no significant excess of γ -like air showers from the position of GRB 050713A above 175 GeV was detected (Albert et al., 2006). This holds both for the prompt emission and during the subsequent observation periods. Figure 8 shows the number of excess events during the first 37 minutes after the burst, in intervals of 20 s. For comparison, the number of expected background events in the signal region, stable and compatible with statistical fluctuations, is shown. Upper limits to the gamma-ray flux are given in Table 3. This is the first observation of the GRB prompt emission phase performed by an IACT.

2.6. Optical and Other Follow-up Observations

Optical followup observations of GRB 050713A performed by the UVOT and by ground based observatories are summarized in Table 4.

The earliest optical afterglow measurement comes from the RAPTOR-S robotic tele-

scope at the Los Alamos National Laboratory in Los Alamos, New Mexico at $R=18.4 \pm 0.18$ in a coadded series of 8×10 second images with a midpoint observation time of $T_0+99.3$ s (Wren et al., 2005). A nearly simultaneous measurement was made by the robotic Liverpool Telescope in a coadded series of $3 \sim 2$ minute exposures in the r' band with a midpoint of observation of T_0+3 minutes (Malesani et al., 2005). Later detections below the Digitized Sky Survey limits were reported within the first 60 minutes after the burst trigger in the R band by the Nordic Optical Telescope (T_0+47 m), in the I band by the Galileo Italian National Telescope in the Canary Islands and in the infrared J, H, and K bands by the Astronomical Research Consortium Telescope at Apache Point Observatory (T_0+53 m).

Due to the bright ($V=6.56$) star HD204408 which is located just 68 arcseconds from the position of the burst, the UVOT background level at the position of the afterglow is significantly higher than usual, resulting in abnormally poor sensitivity of the instrument in detecting the afterglow of GRB 050713A. Considering this high background, the non-detection of the afterglow by the UVOT is not surprising.

All other reported optical observations of the afterglow position have yielded only upper limits. Most of the upper limits are near in time to the actual detections but at brighter magnitudes and thus do not produce strong constraints on the decay rate of the optical afterglow. The R-band measurement made at $T_0+10.3$ hours by the Lulin Telescope in Taiwan, however, is at a sufficiently late epoch to place a useful constraint on the optical decay rate. Fitting a simple powerlaw to the two well defined measurements at $T_0+99.3$ s and T_0+180 s and the upper limit at $T_0+10.3$ hours yields an upper limit on the power law decay slope of $\alpha \geq 0.5$, as is shown in Figure 4.

A radio followup observation made with the VLA reports no detection at $T_0+4.3$ days.

3. Discussion

3.1. Multispectral Lightcurve Overview

The K-W light curve in the 18–1160 keV energy range is similar to the *Swift*-BAT light curve (Fig 1). The small precursor peak detected by BAT at T_0-70 to T_0-50 s is seen by K-W at statistically significant levels in all three broad, pre-trigger bands: G1 (18–70 keV), G2 (70–300), and G3 (300–1160 keV). The other smaller peaks detected by the BAT after the burst trigger are not seen at statistically significant levels in the K-W data, despite the fact that the peaks at T_0+50 s and at T_0+65 s are more intense in the BAT energy range than the precursor is. The detection by K-W of the precursor but not the later flares is indicative of the harder spectral index seen in the precursor as compared to the later flares

(see section 3.3 for discussion of separate spectral fits to individual flares).

The XRT lightcurve with BAT data overplotted is shown in Figure 4. Both the X-ray and gamma-ray data in the first orbit are dominated by flaring activity, making it difficult to draw a conclusion regarding the underlying powerlaw decay index from this orbit alone. The XRT data beginning at T_0+4 ks (orbit 2) and extending until T_0+40 ks show a significantly flatter powerlaw decay slope of $\alpha = -0.8$, implying that a break in the powerlaw decay has occurred near the end of the first orbit of XRT coverage at $T_0+\sim 300$ s and that a period of energy injection occurs from $T_0+\sim 300$ s to $T_0+\sim 15$ ks. Another break in the lightcurve then occurs near T_0+25 ks to a steeper, “normal”, pre-jetbreak decay slope, as shown by the *XMM-Newton* data ($\alpha \sim 1.4$). Support for this notion of the presence of an energy injection phase may be drawn from the harder x-ray spectral slope of the second orbit of XRT data (photon index = 1.9 ± 0.13) compared to the first orbit (photon index = 2.28 ± 0.04), the third orbit (photon index = 2.25 ± 0.23), and the later data (photon index = 2.8 ± 0.6) (Table 5). *XMM-Newton* data coverage nicely fills much of the data gap in the XRT coverage between T_0+15 ks and T_0+40 ks and provides high signal to noise data in this regime, producing a confident determination of the lightcurve break.

The global picture of the lightcurve of this burst is one in which the early data (prior to T_0+12 s) shows a bright plateau in the 15 keV to 1 MeV energy range, consisting of multiple overlapping peaks. At T_0+12 s the emission drops rapidly, consistent with a curvature radiation falloff (Zhang et al., 2005) until subsequent flaring activity begins to be seen in the 0.3–150 keV region with some indication of flux at higher energies from K-W. Due to the rapid rise and decay of the flares, internal shocks from continued central engine activity appears to be the most likely explanation for these flares (Ioka et al., 2005). The earliest ground based optical detections are reported at this time also, suggesting that the flares may also be optically bright. The lack of higher resolution timing information in the optical data, though, admits the possibility that the optical emission may be unassociated with the emission mechanism responsible for the x-ray flares. It is possible that the optical emission is due to synchrotron emission from the reverse shock (RS), though the much higher flux level of the x-ray flare peaks compared to the optical measurements suggests that the x-ray flares themselves are not due to inverse Compton scattering of the optical synchrotron emission of the RS (Kobayashi et al., 2005; Gendre et al., 2005).

Following this prompt emission phase, an energy injection phase begins which dominates the lightcurve until at least T_0+16 ks. During the energy injection phase, continued activity of the central engine adds energy to the afterglow of the burst, either through additional ejection events or through the realization of energy contained in previously ejected outward moving relativistic shells which only collide at later times, producing late time internal shock

emission which is then added to the overall decay (Zhang et al., 2005). It may be expected, if the energy injection phase is due to continued central engine activity, that flaring behavior would continue to be observed during this period and, indeed, some evidence for small scale flaring activity during both the second and third orbit of XRT data can be seen, though at a much reduced significance in comparison to the flaring activity of the first orbit. Near T_0+25 ks, the energy injection phase ends, giving way to a steeper decay slope similar to what is often seen in GRBs after the prompt emission phase and prior to the possible onset of a traditional jet-break (Nousek et al., 2005).

3.2. Flares

Many flares superimposed on top of the overall decay of GRB 050713A show the typical properties seen in other bursts: that $\delta t/t \sim 0.1$ and that the peak flux level is negatively correlated with the time of the flare (Falcone et al., 2006; Barthelmy et al., 2005). These two properties of flares seen in *Swift* GRB afterglows have been cited as evidence for flares being produced through accretion processes onto the central compact object (Perna, Armitage and Zhang, 2006), but we offer here that the constancy of the $\delta t/t$ value of flares may partly be a by-product of the overall decay of the afterglow in so much as the sensitivity of the XRT to flares is naturally degraded as the overall flux level of the afterglow decays, thus *requiring* flares at later times (and hence, lower flux levels) to be longer in duration for enough counts to be collected to produce a significant flare seen above the background. Such a case can be seen in comparing the early time flares in the first orbit of GRB 050713A to the flare seen in the the third orbit. During the first orbit, the underlying flux level beneath the flares is poorly determined, but can be assumed to be 10-100 counts s^{-1} . We are dominated in this portion of the lightcurve by the Poissonian error in the flux, which in a 10 second integration will be 10-32 counts, or 3-10%. Thus, for a flare to appear at the 6 sigma level above the background during this portion of the lightcurve, at most a 60% increase in fluence above the normal powerlaw decay is needed, which can be acquired in a few seconds by the introduction of a flare with twice the flux of the underlying afterglow. During the third orbit, however, the underlying afterglow flux level has dropped to ~ 0.1 counts s^{-1} . During a 10 second integration at 0.1 counts s^{-1} the Poisson error alone is 1 count, so for a flare to be detectable at 6 sigma above background at these count levels, the total fluence must be 6 counts, implying an increase in the rate from 0.1 counts s^{-1} to 0.6 counts s^{-1} during the 10 s interval, a 6 fold increase, which has been seen only in the brighter flares. In order to be sensitive to the same 60% increase in flux level as during the first orbit, the flare which occurs at a flux level of 0.1 counts s^{-1} needs to have a Poission error which is 1/6 of the total counts in the observation, i.e., 36 counts must be collected, which implies

an exposure time of at least 180 s if produced by the introduction of a flare with twice the flux of the underlying afterglow. In other words, because the afterglow flux level decays as $t^{-\alpha}$, the exposure time needed to acquire the same fluence level increases as t^α . Thus, we see that in moving from the first orbit at T_0+100 s to the third orbit at $T_0+10000$ s, assuming a typical underlying powerlaw decay of the afterglow of $\alpha \sim 1$, we have greatly decreased the temporal resolution of XRT to detect flares (from a few seconds to a few hundred seconds). This is not to imply that there is not another more physical cause for the constancy of the $\delta t/t$ ratio seen in flares, but rather to note that the typical GRB seen by the *Swift* XRT does not provide sufficient flux at times typically greater than a few ks to detect the shorter timescale flares that are so often seen during the first orbit.

In GRB 050713A, a hint of emission above the afterglow powerlaw decay appears in the XRT data at T_0+45 ks, though the statistics are, predictably, poor. This time is overlapped by *XMM-Newton* data, though, so we can look for evidence of a short flare in the *XMM-Newton* data at this time. In Figure 9 we show the *XMM-Newton* lightcurve, plotted linearly and zoomed near T_0+45 ks. Though a 1-2 sigma deviation above the background decay is seen at T_0+45 ks, the *XMM-Newton* data appear consistent with a statistical fluctuation rather than a true flare similar to those seen earlier during the burst.

The presence of multiple flares in GRB050713A argues against “one-shot” emission mechanisms such as synchrotron self-Compton emission in a reverse shock or deceleration of the blastwave (Piro 2005a) and it argues in favor of a mechanism which can produce repeated flares, such as late time central engine activity. While it may remain possible that one of the several flares in GRB050713A is due to the RS or the onset of the afterglow due to external shocks, the steep temporal decays of all the temporally fitted flares coupled with the photon indices of the flares ($1.25 \sim 2.5$; Table 6) do not satisfy the closure relations of Sari et al., (1998), Chevalier & Li (1999) and Sari et al., (1999) for propagation of the blast wave into either a wind or constant density ISM. Together these points seem to argue in favor of an internal shock origin for the flares seen in this burst.

3.3. Joint Spectral Fitting

Due to the relatively narrow spectral response function of the BAT (15–150 keV for mask-tagged events) and the XRT (0.3–10 keV), a spectral fit to data from only one of the two high energy instruments on *Swift* is usually not able to discriminate between higher order spectral models. Analysts and authors are usually limited to choosing between a power-law or Band function. In GRB 050713A we have a rare case of data coverage overlap between BAT and XRT (0.3–150 keV) and also between BAT and K-W (15 keV–14 MeV).

Taking advantage of this where appropriate, considering the relative flux levels in the three instruments, we have jointly fitted spectral datasets between the two pairs of instruments. During the precursor and from T_0+0 to $T_0+16.5$ s, we perform joint fitting between BAT and K-W data. From $T_0+16.5$ to T_0+78 s we have only BAT data. From T_0+78 to T_0+116 s and during the onset of the flare at T_0+160 we perform joint fitting between XRT and BAT. We have grouped the data into segments (as shown in Table 6) in order to temporally separate data which we expect may show significantly different spectral parameters. Segments 1-4 contain BAT and K-W data and are segmented to separate the precursor from the prompt emission and the prompt emission from the rapid decay phase. Segment 5 contains BAT data only and segments 6-10 contain XRT and BAT data. These are segmented to distinguish the 3 flares which have overlapping data and also to separate the rise of each flare from the decay of each flare. We attempt fits to each of these segments using 4 different spectral models: 1) an absorbed powerlaw 2) an absorbed cutoff or broken powerlaw (cutoff for data extending beyond 150 keV, broken otherwise) 3) an absorbed Band function and 4) an absorbed blackbody plus powerlaw.

3.3.1. Segment 1: precursor (T_0-65 to T_0-55 s)

The precursor is the most poorly sampled of all the regions. Despite the low number of counts in the region, a cutoff powerlaw is favored over a single powerlaw at 90% confidence according to the F-test. Of all the segments fit, the precursor has the hardest photon index, regardless of the model which is used to perform the fits.

3.3.2. Segment 2: prompt emission plateau (T_0+0 to $T_0+8.5$ s)

The plateau of the prompt emission is best fit by an exponentially cutoff powerlaw model with photon index = 1.26 and $E_{peak} = 421$ keV. Next to the precursor, the prompt plateau has the second hardest photon index of all segments fit, regardless of the model used.

3.3.3. Segment 3: rapid decay ($T_0+8.5$ to T_0+25 s)

As with the other data segments which contain K-W data, the rapid decay segment is poorly fit by a simple powerlaw and is best fit by a cutoff powerlaw or Band function. The photon index of the cutoff powerlaw in segment 3 is quite similar to that in the prompt plateau, but the cutoff energy is somewhat lower (312 keV compared to 421 keV in the

plateau), suggesting that the highest energy flux is “shutting off” during the rapid decay phase.

3.3.4. Segment 4: plateau + early rapid decay (T_0+0 to $T_0+16.5$ s)

This segment is an extension of the prompt segment to slightly later times, encompassing slightly more data. The cutoff powerlaw or Band function is the best fit, with photon indices similar to segment 2 and E_{peak} between that in segments 2 and 3.

3.3.5. Segment 5: rise of T_0+60 s flare (T_0+59 to T_0+68 s)

This segment contains only BAT data and is included for completeness, though the narrowness of the BAT spectral response limits the ability to distinguish between models. A simple powerlaw is a good fit with photon index of 1.83. N_H is unconstrained. The powerlaw plus blackbody model produces a good fit to this segment but only with a very minimal blackbody component, effectively reproducing the fit of the simple absorbed powerlaw. Therefore we consider the powerlaw plus blackbody model inapplicable to this segment.

3.3.6. Segment 6: decay of T_0+60 s flare (T_0+68 to T_0+95 s)

Only in this segment, the data time ranges are mismatched between XRT and BAT (due to XRT observations beginning towards the end of the flare decay). Rather than ignore this flare or consider only the later part of the flare decay where XRT and BAT data coverage overlap, we have chosen to fit the entire BAT time range from T_0+68 to T_0+95 s together with the T_0+79 to T_0+95 s XRT data (note that the Image mode data taken at T_0+73 s are highly piled up and cannot be used spectrally) for consistency with our treatment of the other flares. A simple powerlaw is a good fit to this segment, yielding $N_H = 5.2 \times 10^{21} \text{ cm}^{-2}$ and a photon index of 2.47, significantly softer than the rise of the flare, as expected.

3.3.7. Segment 7: rise of T_0+100 s flare (T_0+100 to T_0+113 s)

In the rise of the brightest flare seen in XRT, both an absorbed powerlaw plus blackbody model and an absorbed broken powerlaw model are significantly better fits (F-test probability 3×10^{-4}) than a simple absorbed powerlaw. The powerlaw plus blackbody indicates $N_H =$

$1.2 \times 10^{22} \text{ cm}^{-2}$ and a relatively soft photon index of 2.0 with a blackbody temperature of $kT = 0.1 \text{ keV}$. We note that this value of kT is below the XRT energy band and may therefore indicate a non-physical spectral solution. The absorbed broken powerlaw indicates $N_H = 4.3 \times 10^{21} \text{ cm}^{-2}$ and photon indices of $\Gamma_1 = 1.26$ and $\Gamma_2 = 2.01$, broken at 3.4 keV. These two models are somewhat degenerate in this dataset, with both models producing a roll over in flux at low (below 0.5 keV) and high (above 50 keV) energies.

3.3.8. Segment 8: decay of $T_0 + 100 \text{ s}$ flare ($T_0 + 113$ to $T_0 + 150 \text{ s}$)

The decay portion of this flare is well fit by a simple absorbed powerlaw with $N_H = 6.0 \times 10^{21} \text{ cm}^{-2}$ and photon index of 2.68. We note, however, that both an absorbed broken powerlaw and absorbed powerlaw plus blackbody are equally good fits to the data.

3.3.9. Segment 9: rise of $T_0 + 160 \text{ s}$ flare ($T_0 + 159$ to $T_0 + 171 \text{ s}$)

The rise of the last flare with overlapping data is well fit by a simple absorbed powerlaw with $N_H = 5.4 \times 10^{21} \text{ cm}^{-2}$ and photon index = 2.52, however the absorbed powerlaw plus blackbody is, strictly, a better fit according to the F-test, though only at about the 80% confidence level (F-test probability = 0.219), with $N_H = 5.0 \times 10^{21} \text{ cm}^{-2}$, $kT = 200 \text{ keV}$ and photon index of 2.43. We note that this value of kT is above the XRT-BAT energy band and may therefore indicate a non-physical spectral solution.

3.3.10. Segment 10: decay of $T_0 + 160 \text{ s}$ flare ($T_0 + 171$ to $T_0 + 200 \text{ s}$)

The decay of this flare is well fit by an absorbed powerlaw with $N_H = 3.8 \times 10^{21} \text{ cm}^{-2}$ and photon index of 2.55, though as with segment 9, the absorbed powerlaw plus blackbody is also an acceptable fit with $N_H = 4.4 \times 10^{21} \text{ cm}^{-2}$, $kT = 5.2 \text{ keV}$ and photon index of 2.83. It should be noted that the BAT flux is very near the noise level in this segment and really provides only an upper limit on the spectral fitting process in the higher energy region.

3.4. Broadband SED

We have produced the broadband SED (spectral energy distribution) of the afterglow of GRB 050713A over the time range from $T_0 + 20 \text{ s}$ to $T_0 + 1000 \text{ s}$ (Fig 10). This timerange

includes detections of the burst afterglow in the optical from the RAPTOR-S and Liverpool telescopes (corrected for the galactic extinction in this direction of $A_R=1.04$ (Schlegel et al., 1998)) and in the X-ray from *Swift* BAT and XRT. It also includes upper limits in the gamma-ray energy range from K-W (whose detectable emission ends at $T_0+\sim 10$ s) and in the GeV energy range from MAGIC. A similar SED has been addressed by the MAGIC collaboration in their paper regarding the MAGIC flux upper limit (Albert et al., 2006) in which they note that the SED composed of data from *Swift* and MAGIC (0.2 keV to 400GeV) is fit by a Band function at low energy and that the MAGIC data are consistent with a single unbroken powerlaw extending from E_{peak} (at ~ 400 keV) to the MAGIC limits up to 500 GeV. We confirm this result, citing a best fit photon index for a single powerlaw fit from 400 keV to 500 GeV of $\Gamma = 2.1 \pm 0.1$ and a reduced $\chi^2_r = 1.66$ for 63 dof. We further note that in performing our fit to the MAGIC data, we have treated the MAGIC upper limits as data points during our fit, thus our photon index of 2.1 is only a lower limit on the true photon index of a powerlaw which would fit the true flux level at GeV energies. Our results here are, therefore, consistent with the analysis of the Albert et. al., in which they show that their data are consistent with a powerlaw photon index of 2.5 from 400 keV to 500 GeV.

We add that a Band function fit is not, however, consistent with the data when we also consider the contemporaneous optical detections. The relative faintness of the optical detections compared to the X-ray detections combined with the upper limits from K-W and MAGIC requires an absorbed broken powerlaw fit. Figure 10 shows the best fit to the entire SED using an absorbed powerlaw (dotted), absorbed broken powerlaw (solid) and absorbed Band function (dashed). The spectral parameters and fit characteristics for each of these fits are shown in Table 7. We have not corrected for the attenuation of flux above 10GeV due to photon-photon interactions with the infrared background (de Jager and Stecker 2002; Kneiske et al., 2004; Primack, Bullock and Somerville 2005), however, our spectral fit results will remain valid independent of this effect due to the constraints placed by the K-W limiting flux measurement from 20 keV to 14 MeV.

4. Summary

GRB 050713A is one of the rare bursts observed simultaneously in soft X-rays (XRT), hard X-rays (BAT) and gamma-rays (K-W). The broad spectral coverage of these simultaneous measurements has allowed us to fit the early prompt emission, rapid decay, and several flares in the early emission with several different spectral models. In general we find a cutoff powerlaw model to be a good fit to segments with data extending into the MeV range, thus able to constrain the high energy component of the model. For data segments

with 0.3–150 keV coverage (BAT and XRT data) we find that a simple absorbed powerlaw is often an adequate fit to the data, though an absorbed powerlaw plus blackbody or absorbed broken powerlaw model seems to sometimes be a marginally better fit during periods of flaring activity.

The lightcurve structure of GRB 050713A is quite typical of many GRBs that have been observed by *Swift*. It has an early section showing steep decay slopes of $\alpha > 5$ and bright flares extending until $T_0 + \sim 1$ ks, followed by a break to a flatter section with decay slope $\alpha \sim 1.0$ lasting until $T_0 + \sim 25$ ks, followed by a break to a steeper slope of $\alpha = 1.45$.

We have temporally separated the early, flaring portion of the burst into 10 segments and attempted to fit each segment using 4 different spectral models: 1) an absorbed powerlaw 2) an absorbed cutoff or broken powerlaw (cutoff for data extending beyond 150 keV, broken otherwise) 3) an absorbed Band function and 4) an absorbed blackbody plus powerlaw. In all segments where at least two instruments provide significant, simultaneous levels of emission, and hence the spectral data span more than 2 decades in energy, we find that at least one of the higher order spectral models is acceptable and, in several cases, is a better fit to the data than a simple absorbed powerlaw. This suggests that the spectral shape of GRB flares, while consistent with a simple absorbed powerlaw when viewed through any particular narrow spectral window, is intrinsically fit in the broadband by a model with attenuated flux above (and possibly below) some threshold energy.

It has long been known that GRB prompt emission is better fit by spectral models with a high (and sometimes low) energy cutoff than by a simple absorbed powerlaw (Ryde 2005; Band et al., 1993), and thus the indication that GRB flares are fit by a similar spectral model suggests that similar emission mechanisms may be responsible for the production of flares and for the prompt emission itself, namely internal shocks produced as a result of central engine activity. Since the discovery of X-ray flares in GRBs by *Swift*, relatively few of the flares have been observed simultaneously across a broad enough energy range to determine whether such higher order models are necessary to fit their spectra, making the multi-instrument observations of GRB 050713A unique and valuable.

We have also examined the temporal properties of the flares seen in GRB 050713A as early as $T_0 + 80$ s and as late as $T_0 + 10$ ks. In all cases we find the flares to have steep powerlaw rise and decay slopes and $0.1 < \delta t/t < 1$, which also suggests internal rather than external shocks as the production mechanism for the flares (Burrows et al., 2005b; Ioka et al., 2005). We have noted that the presence of multiple flares and the failure of those flares to fit the closure relations associated with the external shock in a wind or constant density ISM further argues in favor of the internal shock origin for the flares.

We have furthermore discussed the difficulty that *Swift* XRT will face in detecting late time flaring activity. We have noted that the XRT will have difficulty resolving late, short-timescale flares due to the low XRT count rates typically involved. Data from higher throughput instruments such as *XMM-Newton EPIC* will be important for constraining flares at these times. GRB 050713A has simultaneous coverage at moderately late times with *XMM-Newton EPIC*, but no conclusive evidence of flaring in the *XMM-Newton* data has been found in this case.

Finally, we have created a broadband SED of the flaring region of GRB 050713A from 0.002 keV to 500GeV at times from T_0+20 s to T_0+1000 s. We find that the SED is inconsistent with a single absorbed powerlaw or an absorbed Band function and is best fit by an absorbed broken powerlaw. This overall SED again implies that GRB flares are best fit by a spectral model similar to that of the prompt emission itself and thus suggests a common mechanism for the emission from the prompt phase and from flares.

This work is supported at Penn State by NASA contract NAS5-00136. We gratefully acknowledge the contributions of dozens of members of the *Swift* team at PSU, University of Leicester, OAB, GSFC, ASDC, MPE and our subcontractors, who helped make this Observatory possible and to the Flight Operations Team for their support above and beyond the call of duty. This work contains observations obtained with *XMM-Newton*, an ESA science mission with instruments and contributions directly funded by ESA member states and the USA (NASA). The K-W experiment is supported by Russian Space Agency contract and RFBR grant 06-02-16070.

REFERENCES

- Albert, J., et al., 2006, ApJ, 641, L9-L12
- Aptekar, R.L., et al., 1995, Space Sci. Rev., 71, 265
- Band, D., et al., 1993, ApJ, 413, 231
- Barthelmy, S., et al., 2005, Space Sci. Rev., 120, 143
- Barthelmy, S., et al., 2005, Nature 438, 994
- Burrows, D.N., et al., 2005a, Space Sci. Rev., 120, 165
- Burrows, D.N., et al., 2005b, Science, 309, 1833

Chevalier, R.A., and Li, Z.Y., 1999, ApJ, 520, L29

Dickey, J.M. and Lockman, F.J., 1990, ARA&A. 28, p215

Falcone, A.D., et al., 2005, GCN 3581

Falcone, A.D., 2006, ApJ, 641, 1010

Gallant, Y.A., et al., 1999, A&AS, 138, 549G

Gehrels, N., et al., 2004, ApJ, 611, 1005

Gendre, B., et al., 2005, A&AS, accepted, astro-ph/0603431

Hill, J.E., et al., 2004, Proc. SPIE, Vol. 5165, 217

Hill, J.E., et al., 2005, ApJ, 639, 303

Ioka, K., et al., 2005, ApJ, 631, 429

de Jager, O.C. and Stecker, F.W. 2002, ApJ, 566, 738

Kneiske, T. M., et al., 2004, A&AS, 413, 807

Kobayashi,, S., et al., 2005, astro-ph/0506157

Kraft, R.P., Burrows, D.N., Nousek, J.A., 1991, ApJ, 344, 355

Kouveliotou, C., et al., 1993, ApJ, 413:L101, L104

Malesani, D., et al., 2005, GCN 3582

Mirzoyan, R. et al., 2005, IP Procs 29th ICRC

Nousek, J.A., et al., 2005, ApJ, 642, 389

Palmer, D.M., et al., 2005, GCN 3597

Perna, R., Armitage, P.J., Zhang, B., 2006, ApJ, 636, 29

Piro, L., 2005, ApJ, 623, 314

Piro, L., 2005, astro-ph/0506020

Primack, J.R., Bullock, J.S., Somerville, R.S. 2005, AIP Conf. Proceedings # 745, p23

Romano, P., et al., 2006, A&AS, 450, 59

Roming, P., et al., 2005, *Space Sci. Rev.*, 120, 95

Ryde, F., 2005, *ApJ*, 625, 95

Sari, R., et al., 1998, *ApJ*, 497, L17

Sari, R., and Piran, T., 1999, *ApJ*, 520, 641

Schlegel, D.J., Finkbeiner, D.P., and Davies, M., 1998, *ApJ*, 500, 525

Wren, J., et al., 2005, *GCN* 3604

Zhang, B. and Meszaros, P., 2004, *IJoMP A*, v19, 15, 2385

Zhang, B., et al., 2006, *ApJ*, 642, 354

Table 1. A Summary of High Energy Observations of GRB 050713A

Observatory /Instrument	Start Time (UT)	Stop Time (UT)	Live-time (Seconds)	Time Since BAT Trigger (Seconds)
Swift-BAT	05-07-13-04:29:02.4	05-07-13-04:32:00	178	0
Konus-Wind	05-07-13-04:29:03.1*	05-07-13-04:37:14.8	491.8	0.7
MAGIC(limit)	05-07-13-04:29:42	05-07-13-05:06:45	2223	40
Swift-XRT	05-07-13-04:30:14	05-08-01-04:37:02	167740	72
XMM-Newton	05-07-13-10:17:00	05-07-13-18:22:00	20900	21000

*The Konus-Wind trigger time corrected for the propagation time from Wind to Swift

Table 2. GRB 050713A: X-ray Flares Parameters.

Start Time (s)	Stop Time (s)	Duration (s)	Rise Index α^a (unitless)	Decay Index α^b (unitless)	Peak Flux (ergs cm $^{-2}$ s $^{-1}$)
79	101	22	NA	5.6 ± 1.8	3×10^{-8} (from BAT)
101	161	60	23.3 ± 5	8.4 ± 1.8	9×10^{-9}
161	304	143	8.9 ± 3	6.1 ± 1.2	1.5×10^{-9}
9751	11840	2089	5.76 ± 1.8	11.0 ± 2.4	1×10^{-11}

^aIndex α of a powerlaw fit to the rise of the flare with T_0 =BAT trigger time; $\Gamma_\nu \propto (t-T_0)^\alpha$

^bIndex α of a powerlaw fit to the decay of the flare with T_0 =BAT trigger time; $\Gamma_\nu \propto (t-T_0)^{-\alpha}$

Table 3. MAGIC upper limit (95% CL) on GRB 050713A between $T_0 + 40$ s and $T_0 + 130$ s. Limits include a systematic uncertainty of 30%. 1 C.U. (*Crab Unit*) = $1.5 \times 10^{-6} \times (E/\text{GeV})^{-2.58} \text{ ph cm}^{-2} \text{ s}^{-1} \text{ GeV}^{-1}$.

Energy (GeV)	Excess evts. (uplim)	Eff. Area ($\times 10^8 \text{ cm}^2$)	Flux lim ($\text{cm}^{-2} \text{ keV}^{-1} \text{s}^{-1}$)	Flux lim (C.U.)
175 – 225	8.5	1.7	1.3×10^{-17}	7.6
225 – 300	10.4	3.4	3.9×10^{-18}	4.8
300 – 400	6.0	5.3	1.6×10^{-18}	3.8
400 – 1000	4.3	6.5	2.3×10^{-19}	3.3

Table 4. GRB 050713A: Ground Based Optical and Radio Followup.

Observatory	Time	Band	Magnitude/Limit
McDonald Obs, Tex	$T_0+22.4$ s	unfilt	17.7 (lim)
RAPTOR-S, LANL	$T_0+99.3$ s	R	18.4 ± 0.18
Liverpool Robotic Telescope, Canary Islands	T_0+180 s	r'	19.2
<i>Swift</i>	T_0+252 s	V	17.98
<i>Swift</i>	T_0+309 s	U	17.81
<i>Swift</i>	T_0+311 s	UVM2	17.13
<i>Swift</i>	T_0+325 s	UVW1	16.85
<i>Swift</i>	T_0+326 s	UVW2	17.08
<i>Swift</i>	T_0+351 s	B	18.08
Red Buttes Obs, Wy	T_0+27 m	R	19.4 (lim)
Red Buttes Obs, Wy	T_0+31 m	I	18.2 (lim)
Nordic Optical Tel	T_0+47 m	R	< DSS limit
Galileo National Telescope, Canary Islands	T_0+48 m	I	< DSS limit
ARC Telescope, Apache Point Obs	T_0+53 m	J,H,K	detected
Red Buttes Obs, Wy	T_0+93 m	R	19.4 (lim)
Red Buttes Obs, Wy	T_0+98 m	I	18.7 (lim)
Lulin Telescope, Taiwan	$T_0+10.3$ h	R	22.4 (lim)
VLA, NRAO	$T_0+4.3$ d	8.5 GHz	96 microJan

Table 5. Swift and *XMM-Newton* spectral fits pre-break and post-break.

Observatory	photon index	N_H (cm^{-2})	comment
<i>Swift</i> orbit 1	2.28 ± 0.04	$4.8 \pm 0.2 \times 10^{21}$	pre- energy injection phase
<i>Swift</i> orbit 2	1.90 ± 0.13	$3.1 \pm 0.4 \times 10^{21}$	energy injection phase
<i>Swift</i> orbit 3	2.25 ± 0.23	$4.1 \pm 0.7 \times 10^{21}$	flare during energy injection
<i>Swift</i> after orbit 3	2.8 ± 0.6	$5.6 \pm 0.2 \times 10^{21}$	post-break
<i>XMM-Newton</i>	2.1 ± 0.05	$3.0 \pm 0.1 \times 10^{21}$	post-break

Table 6. GRB 050713A: Joint Spectral Fits - We group the data into segments to separate times which may show different spectra. Segments 1-4 contain BAT and K-W data and are segmented to separate prompt emission from the rapid decay phase. Segment 5 contains BAT data only and segments 6-10 contain XRT and BAT data. These are segmented to separate the rise and decay of each flare. We attempt fits to each segment using 4 spectral models: 1) an absorbed powerlaw 2) an absorbed cutoff or broken powerlaw 3) an absorbed Band function and 4) an absorbed blackbody plus powerlaw. In segments where a particular model was inapplicable or the fit did not converge, NA is entered in the table.

segment	1	2	3	4	5	6	7	8	9	10
δt (s)	-70 - -49.5	0-8.5	8.5-25	0-16.5	59-68	68-95	100-113	113-150	159-171	171-200
Instr	BAT	and	K-W		BAT		XRT	and	BAT	
pl:N _H	NA	NA	NA	NA	NA	0.52	0.59	0.60	0.54	0.38
pl:PhInd	1.26	1.44	1.61	1.47	1.83	2.47	1.72	2.68	2.52	2.55
pl: χ^2_ν	1.54	1.96	1.39	1.95	0.98	1.20	1.21	1.07	1.04	1.00
pl:dof	12	101	91	98	26	74	98	125	22	37
cutoffpl:PhInd	0.913	1.26	1.31	1.25	NA	NA	NA	NA	NA	NA
cutoffpl:E _{peak}	270	421	312	400	NA	NA	NA	NA	NA	NA
cutoffpl: χ^2	1.20	1.60	1.02	1.29	NA	NA	NA	NA	NA	NA
cutoffpl:dof	11	110	90	100	NA	NA	NA	NA	NA	NA
bknpl:N _H	NA	NA	NA	NA	NA	0.58	0.43	0.45	NA	NA
bknpl:PhInd1	NA	NA	NA	NA	0.95	2.69	1.26	1.93	NA	NA
bknpl:E _{break}	NA	NA	NA	NA	5.8	4.1	3.4	1.8	NA	NA
bknpl:PhInd2	NA	NA	NA	NA	2.1	1.5	2.0	2.8	NA	NA
bknpl: χ^2_ν	NA	NA	NA	NA	1.06	1.31	1.03	1.04	NA	NA
bknpl:dof	NA	NA	NA	NA	23	73	97	124	21	36
Band:N _H	NA	NA	NA	NA	NA	0.33	0.49	0.54	0.41	0.33
Band: α	-1.13	-1.27	-1.27	-1.29	-2.01	-1.69	-1.46	-2.32	-1.98	-2.17
Band: β	-1.26	-9.36	-2.39	-9.29	-9.07	-1.88	-9.36	-9.32	-9.04	-8.78
Band:E _{peak}	101	761	244	636	994	10.6	30.7	10.6	10.6	10.6
Band: χ^2_ν	1.85	1.61	1.03	1.28	1.06	2.11	1.11	1.13	1.26	1.12
Band:dof	10	109	89	101	23	73	97	124	21	36
pl+bb:N _H	NA	NA	NA	NA	NA	0.59	1.17	0.63	0.50	0.44
pl+bb:kT	3.59	59.4	26.4	44.97	NA	7.1	0.1	4.4	200	5.2
pl+bb:bb _{norm}	0.068	2.74	0.46	1.47	NA	0.07	2.48	0.01	2.90	0.01
pl+bb:PhInd	1.00	1.64	1.76	1.63	NA	2.75	2.00	2.77	2.43	2.83
pl+bb:pl _{norm}	0.053	13.97	7.69	11.65	NA	1.53	2.32	2.03	0.51	0.44
pl+bb: χ^2_ν	1.15	1.79	1.03	1.60	NA	1.33	1.04	1.07	0.90	0.98
pl+bb:dof	10	109	89	101	NA	73	97	124	21	36

Table 7. GRB 050713A: SED Fit Data - A broadband SED (R-band optical data points to 500GeV upper limits) has been created and we show the result of fits of 3 spectral models: 1) an absorbed powerlaw 2) an absorbed broken powerlaw and 3) an absorbed Band function. We do not report errors on the parameters in the powerlaw fit or Band function because these models are clearly unacceptable as shown by the large values of χ^2_ν . Only the broken powerlaw is an acceptable fit to the entire SED.

Model:Param	Value
pl:N _H	$4.3 \times 10^{21} \text{ cm}^{-2}$
pl:PhInd	2.14
pl: χ^2_ν	10 (65 dof)
bknpl:N _H	$2.9 \pm 0.3 \times 10^{21} \text{ cm}^{-2}$
bknpl:PhInd1	1.1 ± 0.1
bknpl:E _{break}	$1.3 \pm 0.2 \text{ keV}$
bknpl:PhInd2	2.2 ± 0.1
bknpl: χ^2_ν	1.20 (63 dof)
Band:N _H	$2.1 \times 10^{21} \text{ cm}^{-2}$
Band: α	-1.3
Band: β	-2.2
Band:E _{peak}	10.6 keV
Band: χ^2_ν	2.97 (63 dof)

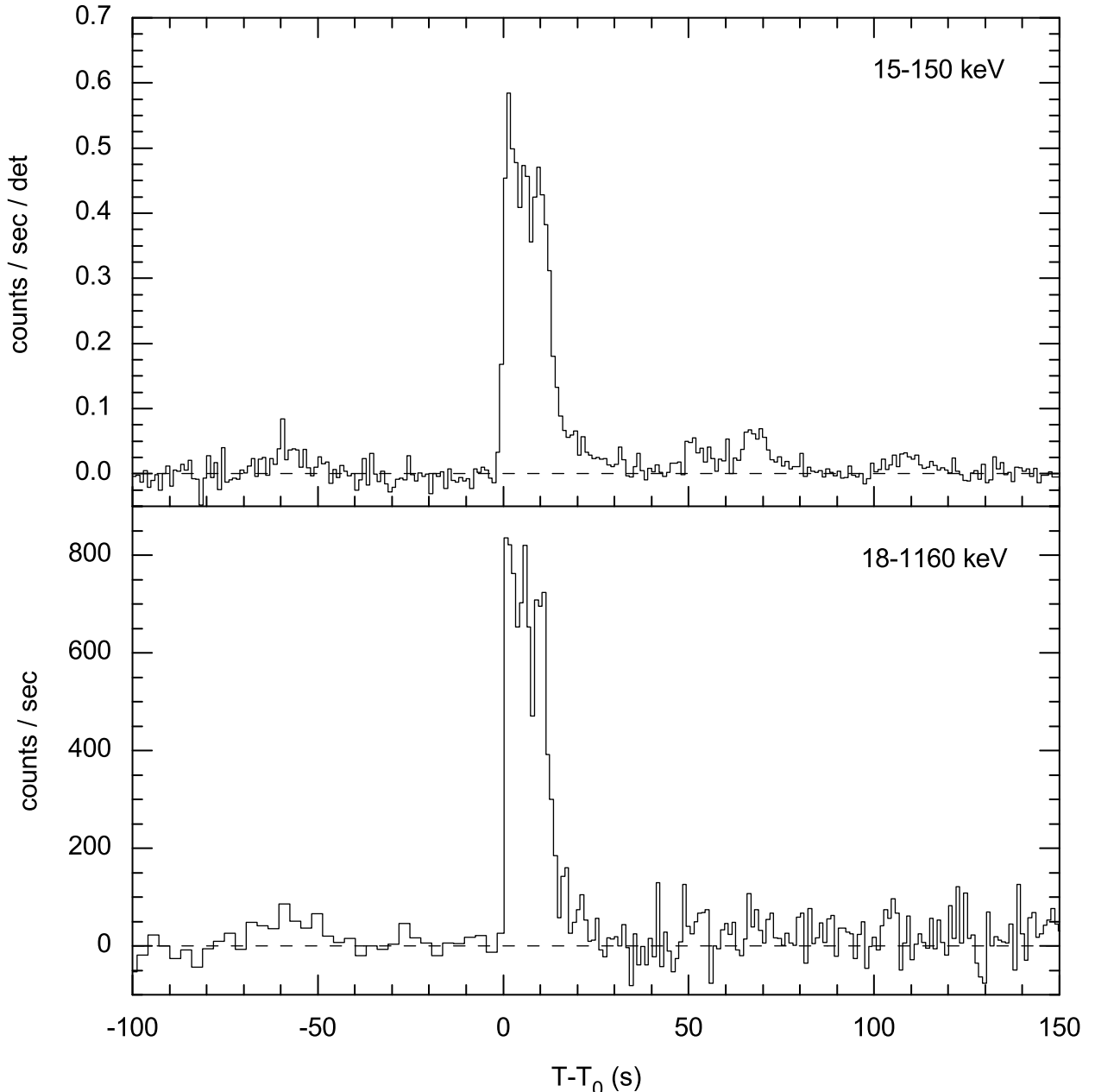


Fig. 1.— Background subtracted BAT (top panel) and Konus-WIND (bottom) light curves on the same time scale. The plots have been adjusted so that the trigger time for both plots is the same relative to the burst. T_0 in the lower plot is $T_0(\text{BAT})$ plus the propagation time between the spacecrafats (0.742 s). BAT data are binned to 1 s resolution throughout. K-W data are binned to 2.94 s resolution in survey mode prior to the burst trigger and are binned to 1 s resolution in GRB follow-up mode after the trigger. Note that the precursor at $T_0 - 65$ s is detected in both BAT and K-W while post-trigger flares seen in the BAT at $T_0 + 50$ s, $T_0 + 65$ s and $T_0 + 105$ s are not clearly detected by K-W. This suggests a harder spectrum for the precursor than the post-trigger flares, which is confirmed by joint BAT/K-W spectral fits. The main burst consists of 3 closely spaced, overlapping pulses in both the BAT and K-W energy ranges. The K-W lightcurve decays rapidly to background level by $T_0 + 15$ s while the BAT lightcurve continues to show low level emission out to $T_0 + \sim 200$ s.

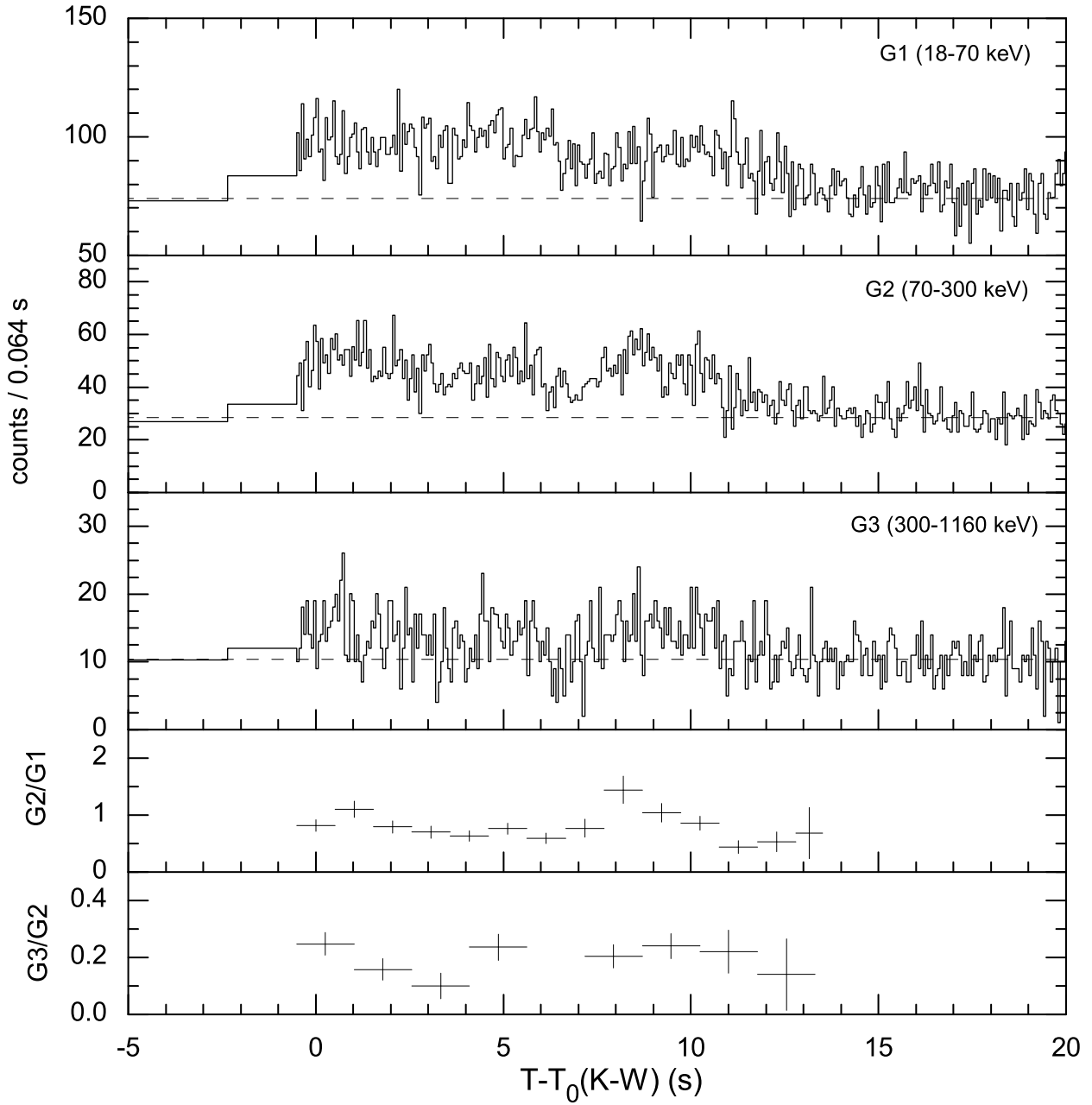


Fig. 2.— Plot of Konus-Wind data in 3 bands and associated band ratios during burst prompt emission. Data binning is 64ms.

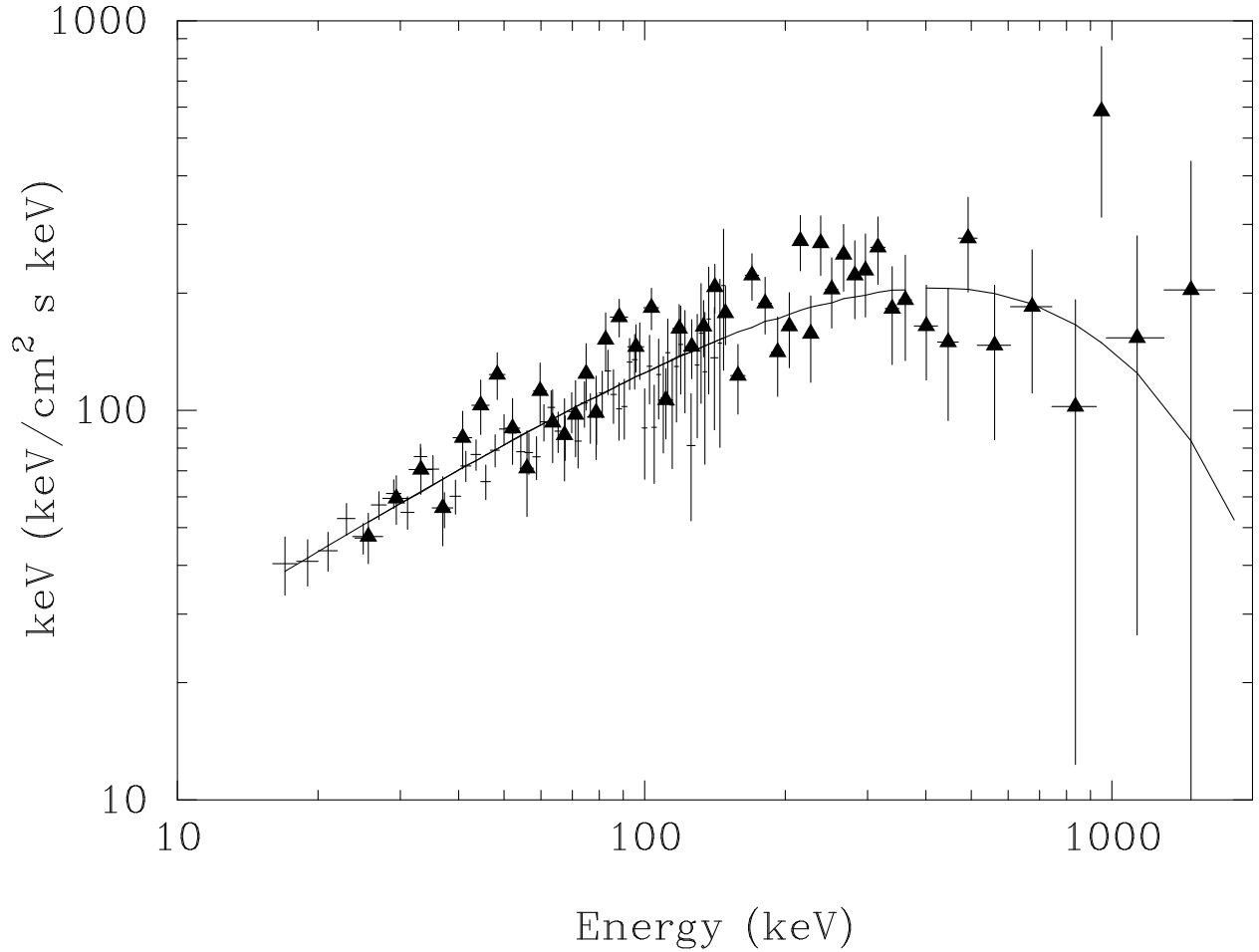


Fig. 3.— Plot of joint spectral energy distribution of Konus-Wind and BAT data during burst prompt emission, showing $E_{peak} = 421$ keV. K-W data are filled triangles, BAT data are crosses. Data channels have been grouped where appropriate to produce significant data points.

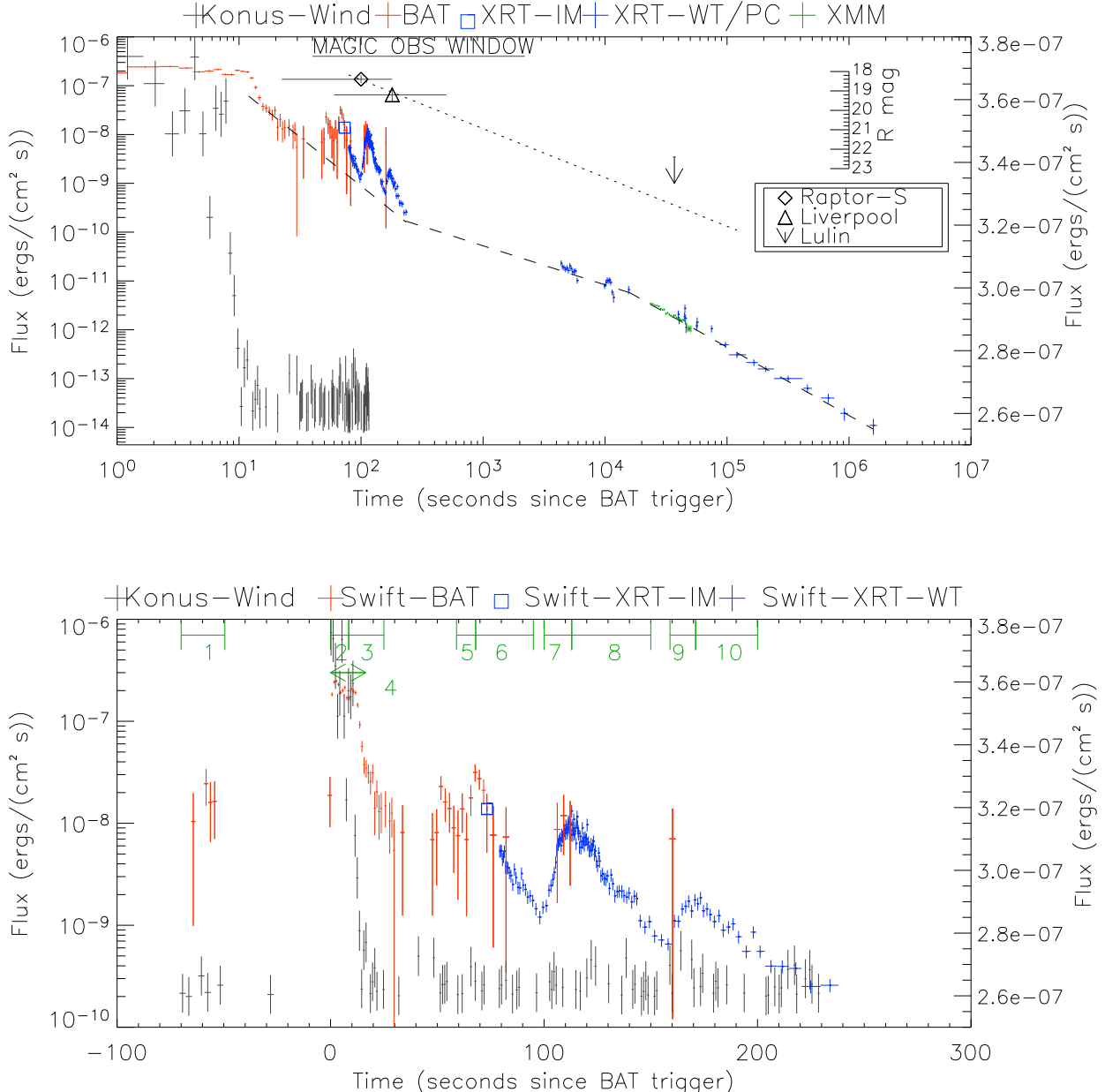


Fig. 4.— X-ray/gamma-ray/optical lightcurve of GRB 050713A. Top: multicolored points are *Swift* and XMM data scaled to the left Y-axis. Black crosses are K-W data scaled to the right Y-axis. Fluxes are extrapolated into the 0.2–10 keV energy range. The diamond, cross and arrow are optical observations and scaled to the inset Y-axis. The scaling of the inset Y-axis is consistent with the outer, left Y-axis such that 1 magnitude is equal to a factor of 2.5 in flux. The window of MAGIC observations is shown by the horizontal bar. The dashed line is the supposed underlying powerlaw decay. Data from T_0+4 ks to T_0+16 ks are well fit by a flatter powerlaw of slope $t^{-0.8}$, implying an energy injection phase. A break to a steeper decay of $t^{-1.45}$ occurs at $T_0+\sim 25$ ks. We note the similar decay slopes in each of the three flares seen by XRT. Optical data are plotted with a fitted powerlaw decay of $t^{-1.0}$. Bottom: a close-up of the flares. Green bars indicate the segments of joint spectral fits.

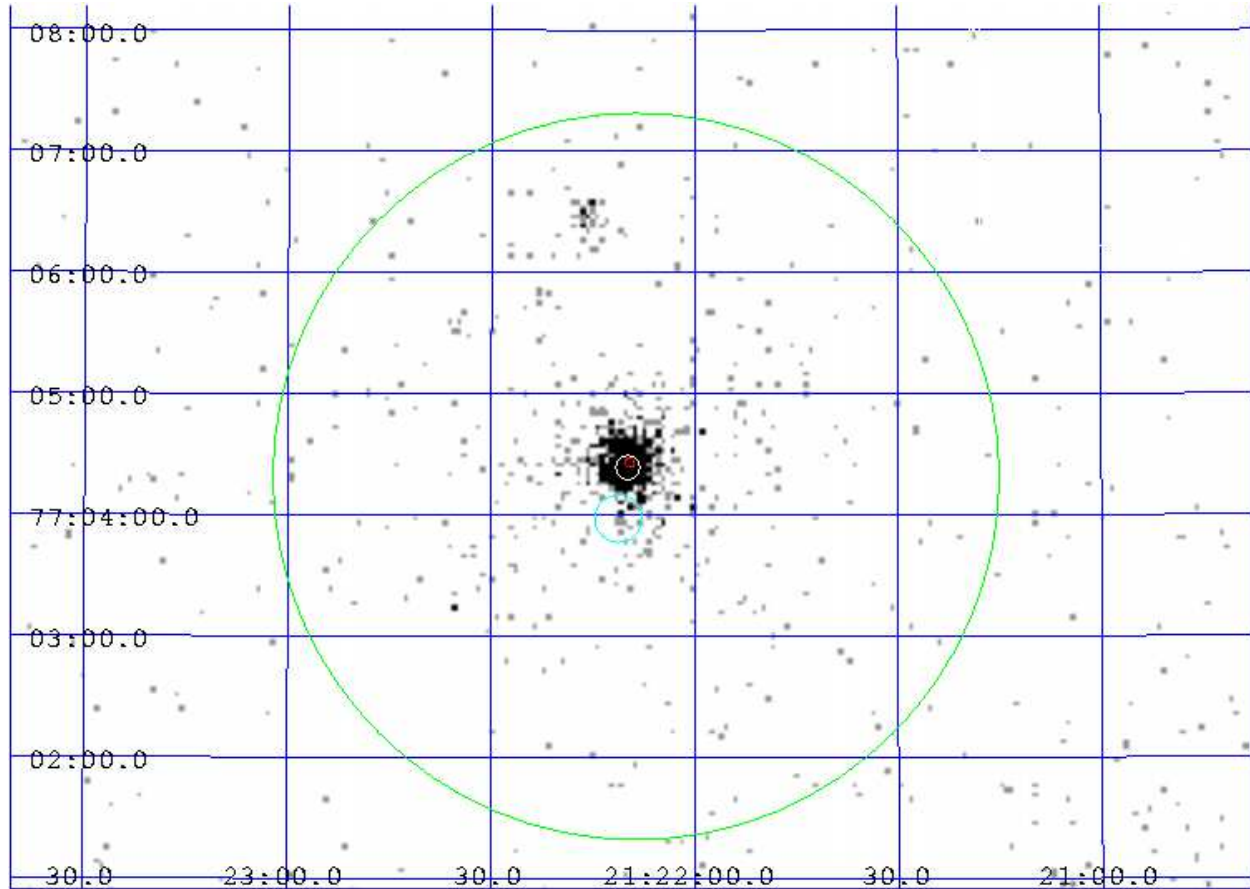


Fig. 5.— XRT image with BAT and XRT optical error circles plotted. Green = BAT; White=XRT; Red=optical. The light blue circle indicates the location of the serendipitous source located 30 arcseconds south of the GRB which has been subtracted from the data.

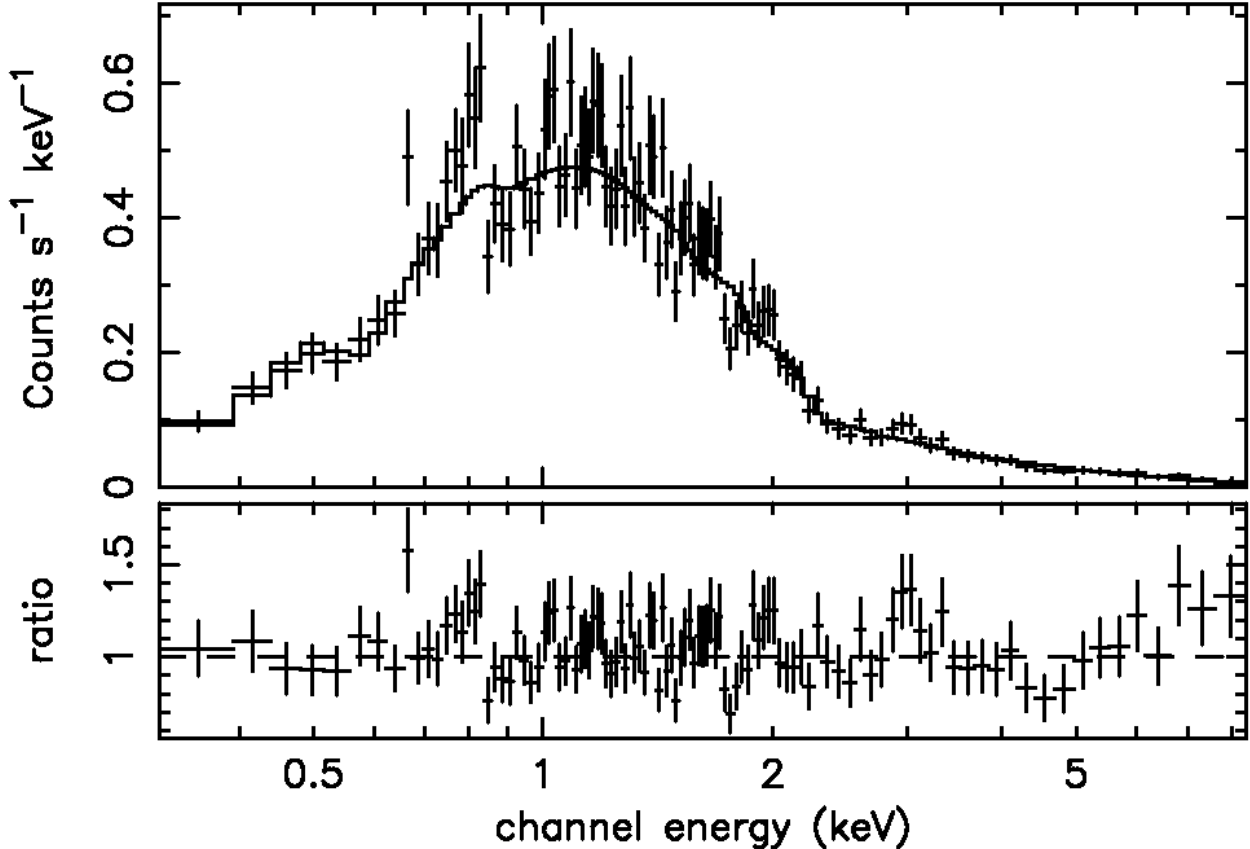


Fig. 6.— PN spectrum from the first 8 ks of the *XMM-Newton* observation. The top panel shows the PN data (crosses) with best fit model (solid line) overlaid, which consists of an absorbed power-law with photon index = 2.07 and $N_{\text{H}} = 3.2 \times 10^{21} \text{ cm}^{-2}$. The bottom panel shows the data/model ratio residuals to this continuum model. A weak excess of counts is seen near 0.8 keV and 3 keV, although if interpreted as emission lines, the detection is not significant.

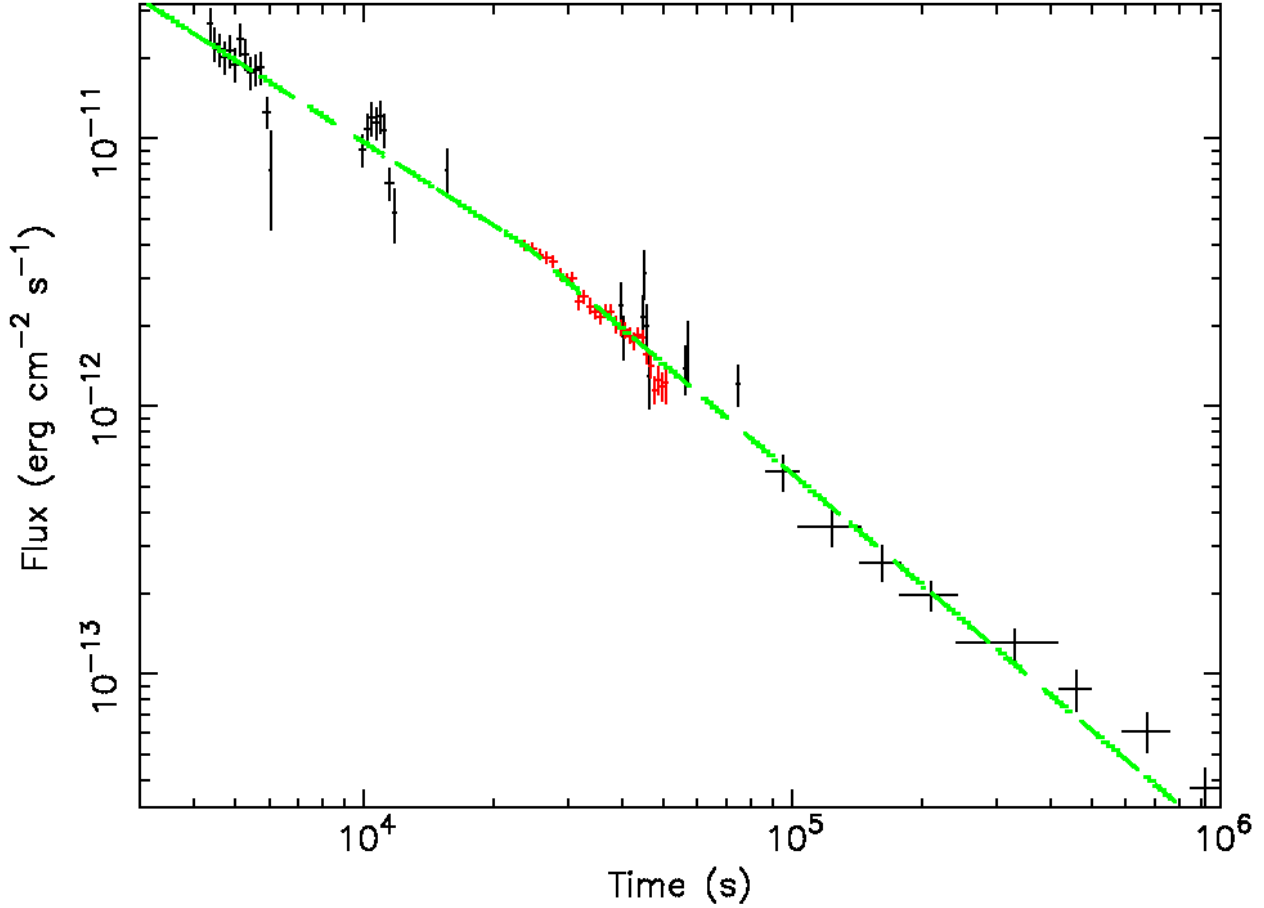


Fig. 7.— Joint *Swift* XRT and *XMM-Newton* PN lightcurve. *Swift* data are from T_0+4 ks to T_0+1000 ks. *Swift* XRT points are shown in black and *XMM-Newton* as red. The afterglow flux is measured in the 0.5–10 keV band, not correcting for absorption. The solid line plotted to the different segments of data is a broken power-law decay model, outlined in the text. The *XMM-Newton* decay index ($\alpha = 1.45$) is considerably steeper than in the XRT at earlier times ($\alpha = 1.0$), suggesting that a break occurs in the lightcurve decay at around T_0+25 ks.

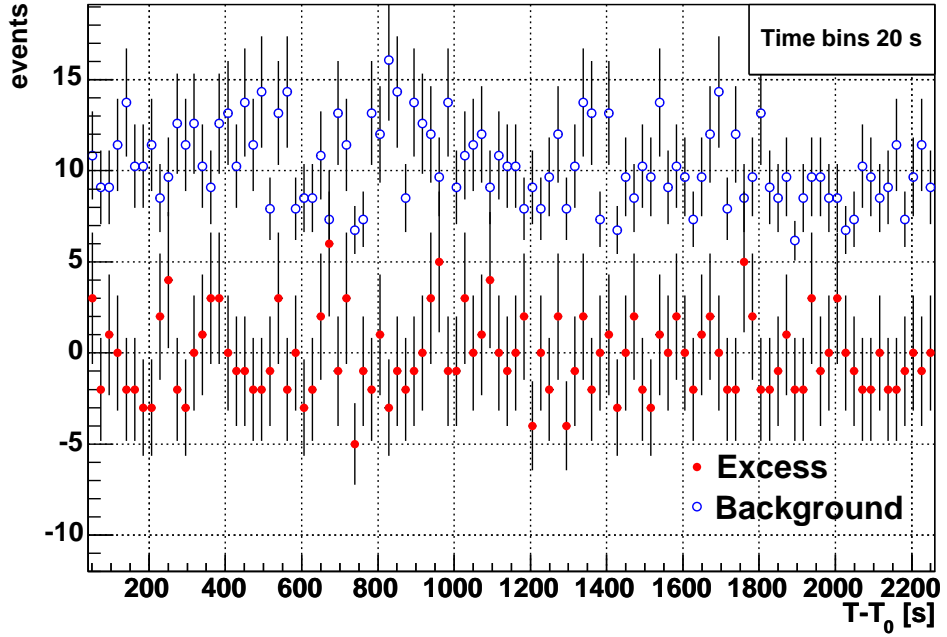


Fig. 8.— MAGIC Observations. Filled circles: number of excess events for 20 s intervals, in the 37 min window after the burst onset. Open circles: number of background events in the signal region. No significant source signal is detected above the background.

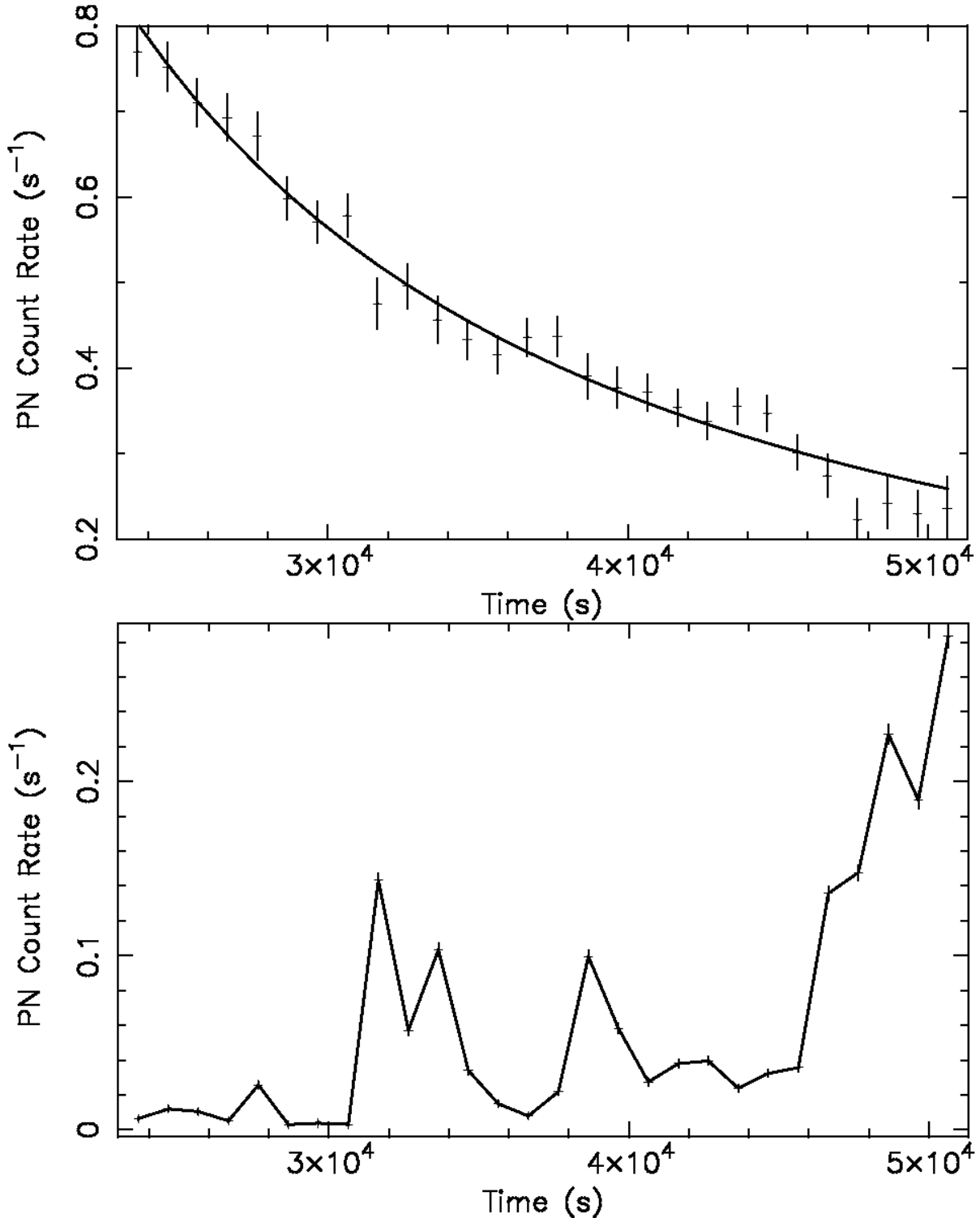


Fig. 9.— *XMM-Newton* lightcurves for the afterglow of GRB 050713A. The top panel shows the background subtracted afterglow lightcurve for the PN detector. Crosses show the GRB source counts (1σ errors), the solid line shows the best fit decay rate of $t^{-1.45}$. Time is plotted compared to the initial BAT trigger. The bottom panel shows the background lightcurve for the PN, normalized to the size of the source extraction region for comparison.

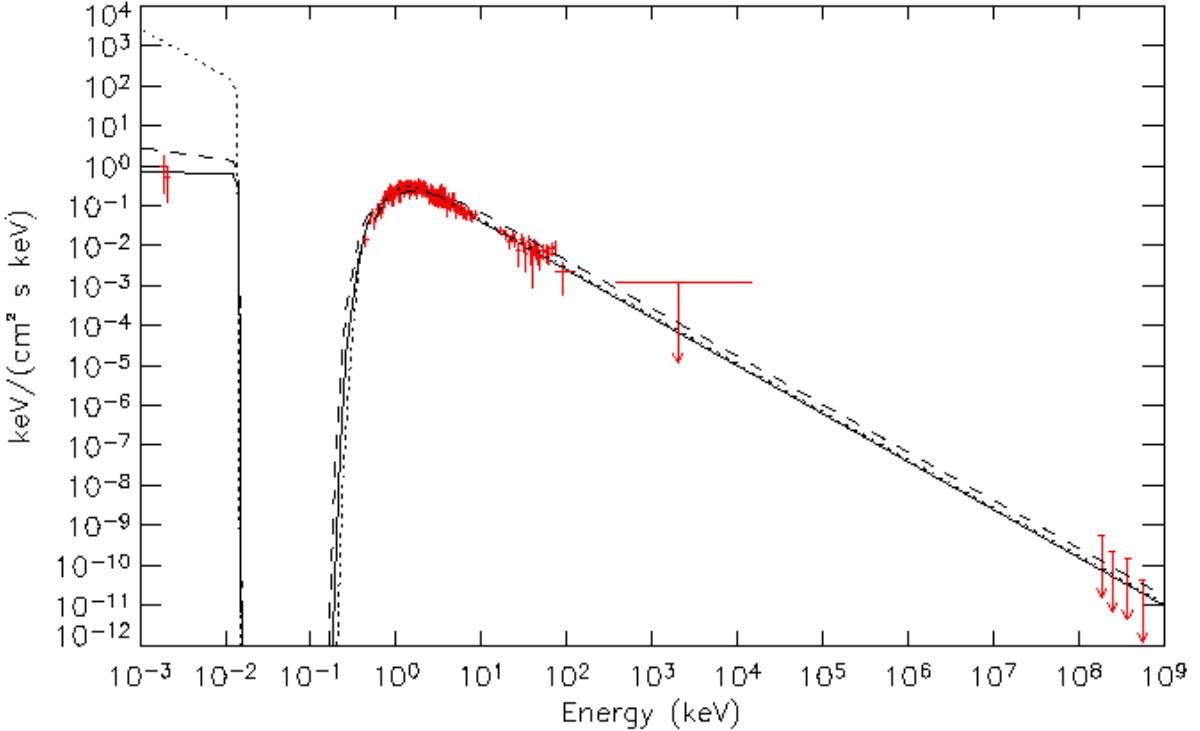


Fig. 10.— Combined multi-platform SED of the early afterglow of GRB 050713A from T_0+20 s to T_0+1000 s. Optical data are from RAPTOR-S at LANL and the Liverpool robotic telescope, soft X-ray (0.2–10 keV) data are from *Swift* XRT, hard X-ray (15–150 keV) data are from *Swift* BAT and gamma-ray upper limits are from Konus-Wind (0.5–14 MeV) and MAGIC (175–500 GeV). The three lines plotted over the data represent the 3 models discussed as proposed fits to the SED in the text. The absorbed broken power law (solid) is the only acceptable fit. The absorbed Band function (dashed) and simple absorbed powerlaw (dotted) do not appear reconcilable with the data. The results suggest that the GRB flare emission is characterized by a single mechanism well represented by a broken powerlaw, or that a more complex, possibly multi-component emission mechanism is required to explain the complete SED.